CHEMICAL PHYSICS

Understanding the density maximum of water with machine-learned potentials

Yizhi Song[1]*, Renxi Liu[1], Chunyi Zhang[1,2], Yifan Li[3], Biswajit Santra[1]†, Mohan Chen[4,5], Michael L. Klein[6,7], Xifan Wu[1,6]*

After melting, at ambient pressure, the density of water continues to increase with temperature until it reaches a maximum around 4°C. For nearly a century, this phenomenon has been qualitatively attributed to a mixture of ordered and disordered structures. Here, we use a deep neural network to train a machine-learned (ML) interatomic potential for water using electronic structure data from advanced density functional theory. Notably, molecular dynamics simulations with the ML potential reproduce both the experimental water density anomaly and the thermal expansion coefficient. Detailed structural analysis of the computed hydrogen-bond network reveals that the density anomaly arises from an emergent liquid structure that retains nearly ideal tetrahedral coordination at short range but collapses at intermediate range. Our findings point to a more delicate mechanism causing the density maximum than the conventional picture, emphasizing the collective roles of structural orderings at different length scales.

INTRODUCTION

Among water's many unique properties, its density anomaly is arguably the most substantial and consequential (*1*). Unlike typical liquids, water becomes denser upon heating from its melting point, reaching a maximum near 4°C before decreasing in density with further warming. This nonmonotonic behavior has profound ecological implications. On a more fundamental level, the anomaly challenges conventional liquid-state theories and has inspired previously unidentified theoretical models for network-forming liquids, pushing the boundaries of classical physics.

The density anomaly remained poorly understood until the seminal work of Bernal and Fowler in 1933 (*2*), which provided the first microscopic structure model. They proposed that water's anomalous behavior stems from its hydrogen-bond (H-bond) network, which at low temperatures forms an ordered, icelike structure characterized by large open volumes and low density. As temperature rises, thermal fluctuations disrupt the H-bonds, transforming the network into a more disordered configuration, thereby enabling denser molecular packing. The Bernal-Fowler model laid the conceptual foundation for later developments based on computer simulations and experiments (*3*–*11*), which describes liquid water as a dynamic mixture of low-density, tetrahedral-like and high-density, disordered local structures, associating the anomalies with a liquid-liquid critical point (*3*, *10*–*15*).

Despite these advances, the microscopic origin of density anomaly remains unresolved and actively debated (*9*, *16*–*19*). The hypothesized liquid-liquid critical point is not directly accessible through experiment (*20*), necessitating reliance on computational investigations. In statistical theory (*7*–*9*, *12*), free energies are typically modeled using order parameters (*21*–*23*) that characterize local structures within the H-bond network responsible for density fluctuations, classifying local structures into low-density and high-density states. However, the microscopic features identified and the population fraction assigned to each structural type are highly sensitive to the choice of structural descriptor (*23*, *24*). This sensitivity highlights the need for a precise understanding of how water molecules are locally packed within the H-bond network to unambiguously link microscopic structure to density fluctuations.

Ab initio molecular dynamics (AIMD) (*25*) based on density functional theory (DFT) (*26*, *27*) provides a rigorous quantum mechanical framework for probing water's behavior (*8*, *28*–*32*), but its high computational cost has traditionally limited its application. Recent advances in machine learning (*33*–*36*) now enable large-scale simulations with DFT-level accuracy (*37*, *38*). While promising, these models have often predicted temperatures of maximum density (TMD) below the melting point (*18*, *39*), contradicting experiment. This discrepancy underscores the highly delicate nature of H-bond network and the continuing need for advanced theories.

Here, we address the microscopic origin of water's density anomaly using large-scale molecular simulations based on the deep potential framework (*34*–*36*). A deep neural network potential, trained on data from a van der Waals (vdW)–inclusive hybrid PBE0 functional (*40*–*44*), is used to simulate water.

RESULTS

As shown in Fig. 1A, we present the predicted water density as a function of temperature relative to its melting point, with experimental data (*45*, *46*) included. A clear nonmonotonic behavior is observed, and the curvature of the simulated density-temperature curve closely follows experimental results across both the supercooled region and temperatures above the melting point. This accurately captured nonlinearity is further supported by the isobaric thermal expansion coefficient α_v shown in the inset of Fig. 1A, which exhibits excellent agreement with experiments (*45*, *46*). In both the simulated density and thermal expansion curves, the density anomaly is identified at

[1]Department of Physics, Temple University, Philadelphia, PA 19122, USA. [2]Eastern Institute of Technology, Ningbo, Zhejiang 315200, P. R. China. [3]Department of Chemistry, Princeton University, Princeton, NJ 08544, USA. [4]HEDPS, CAPT, College of Engineering and School of Physics, Peking University, Beijing 100871, P. R. China. [5]Academy for Advanced Interdisciplinary Studies, Peking University, Beijing 100871, P. R. China. [6]Institute for Computational Molecular Science, Temple University, Philadelphia, PA 19122, USA. [7]Department of Chemistry, Temple University, Philadelphia, PA 19122, USA.
*Corresponding author. Email: yizhi.song@unt.edu (Y.S.); xifanwu@temple.edu (X.W.)
†Present address: Schrödinger Inc., New York: 1540 Broadway, New York, NY 10036, USA.

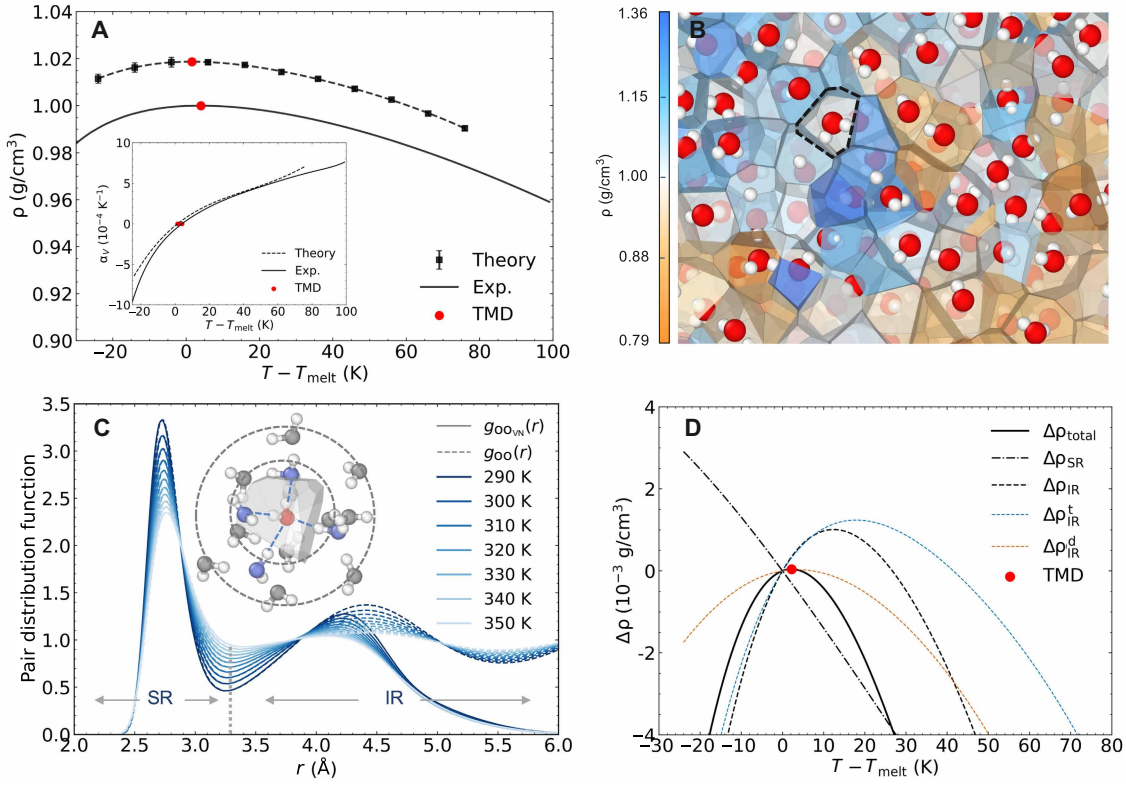

Fig. 1. Structural decomposition of water's density anomaly. (**A**) Temperature-dependent water density and thermal expansion coefficient (inset) from theory and experiment (*45*, *46*). Red circles indicate the TMD. All curves are horizontally shifted by the melting temperature (314.0 K). (**B**) Snapshot of liquid water at 330 K (~16 K above the melting point), with Voronoi cells color coded by local density. The color scale ranges from low local density (orange) to high local density (blue). A representative Voronoi cell is highlighted with a black outline. (**C**) Oxygen-oxygen pair distribution functions (PDFs), $g_{OO}(r)$ (dashed lines), and the corresponding partial contributions from Voronoi neighbors, $g_{OO_{VN}}(r)$ (solid lines). Colors indicate different simulation temperatures. Inset shows a representative Voronoi cell (gray polyhedron) of a central water molecule (red); neighbors forming H-bonds with the center molecule are marked in blue, and others in gray. The two gray circles indicate the first and second coordination shells, respectively. (**D**) Decomposition of the total density change $\Delta\rho_{total}$ into short-range (SR) ($\Delta\rho_{SR}$) and intermediate-range (IR) ($\Delta\rho_{IR}$) contributions. The IR component is further divided into contributions from tetrahedral ($\Delta\rho^{t}_{IR}$) and disrupted tetrahedral ($\Delta\rho^{d}_{IR}$) structures, as defined in Eq. 3. Exp., experiment.

TMD of 1.5 K above the melting point = 314.0 K, with a corresponding maximum density ρ_{max} = 1.02 g/cm^3. The corresponding experimental reference values of the TMD and maximum density are 3.98°C and 1.00 g/cm^3, respectively (*45*). By contrast, other exchange-correlation functionals, such as revPBE0-D3, tend to overestimate the difference between TMD and melting point (≈10 K) (*47*), while BLYP-vdW incorrectly predicts their relative order (*18*).

Decomposition of local density changes

Macroscopically, the observed density is an ensemble average over local fluctuations driven by thermal motion. To resolve these, we use the Voronoi method (*48*, *49*), which partitions the water into space-filling polyhedra centered on the oxygen atoms. The boundaries of each cell are defined by perpendicular bisecting planes between a given central oxygen and its Voronoi neighbors. This geometric construction assigns to each water molecule i a unique local volume V_i, from which the local density is calculated as $\rho_i = m/V_i$, where m is the molecular mass of a water molecule. The macroscopic density is then given by $\rho = m/\langle V\rangle$, where $\langle V\rangle$ is the ensemble-averaged local volume (*50*). Accordingly, variations in the macroscopic density are related to the mean local volume as $\delta\rho = -\frac{m}{\langle V\rangle^2}\delta\langle V\rangle$. Figure 1B shows a representative Voronoi tessellation and the corresponding distribution of ρ_i from an equilibrated snapshot at 330 K. As expected, pronounced spatial inhomogeneity is observed, with broad fluctuations in ρ_i.

Furthermore, the local density ρ_i of a given water molecule depends crucially on the spatial distribution of its Voronoi neighbors. In Fig. 1C, we present the pair distribution function (PDF) between a central oxygen atom and the oxygen atoms of its Voronoi neighbors, alongside the overall oxygen-oxygen PDF for comparison. The Voronoi neighbors consist of all molecules from the first coordination shell and the interstitial region, with only partial contributions from the second coordination shell in Fig. 1C. As the distance from the central molecule increases, the number of Voronoi neighbors decays rapidly and vanishes near ~6 Å consistent with the theoretical density-density correlation length (*51*).

The Voronoi-based analysis above indicates that the local density is determined by the packing of water molecules in the H-bond network at both short range (SR) and intermediate range (IR). Compared to the tetrahedral structure formed by intact H-bonds in ice, the H-bond network in water is highly dynamic. Under thermal fluctuations, H-bonds continuously break and reform on the picosecond timescale (*52*, *53*), yielding a partially collapsed H-bond network. At SR, the structure of the H-bond network can be described by either a near-tetrahedral structure with four H-bonds (see inset

of Fig. 1C) or a disrupted tetrahedron with one or more broken H-bonds, centered on a water molecule. Because of these clear structural characteristics at SR, each water molecule in the equilibrated trajectory can be unambiguously assigned to either a tetrahedral or a disrupted tetrahedral structure, with corresponding Voronoi cell volumes $\langle V_t \rangle$ and $\langle V_d \rangle$ and local densities $\langle \rho_t \rangle$ and $\langle \rho_d \rangle$, respectively. Accordingly, the ensemble-averaged local volume $\langle V \rangle$ can be rigorously decomposed as

$$\langle V \rangle = n_t \langle V_t \rangle + (1 - n_t) \langle V_d \rangle \quad (1)$$

where n_t and $1 - n_t$ denote the fractions of water molecules adopting tetrahedral and disrupted tetrahedral structures, respectively. To separate the contributions from SR and IR ordering in the H-bond network to the overall density variation, we apply a constrained variational decomposition method to the macroscopic density ρ as follows

$$\delta\rho = A \left[\underbrace{(\langle \rho_t \rangle - \langle \rho_d \rangle)\delta n_t}_{\text{SR}} + \underbrace{n_t k \ \delta\langle \rho_t \rangle + (1 - n_t)\frac{1}{k} \ \delta\langle \rho_d \rangle}_{\text{IR}} \right] \quad (2)$$
$$= \delta\rho_{SR} + \delta\rho_{IR}^{t} + \delta\rho_{IR}^{d}$$

Here, $\delta\rho_{SR}$ quantifies the contribution from changes in the population fraction of tetrahedral structures, δn_t, which is governed solely by SR H-bond ordering. The terms $\delta\rho_{IR}^{t}$ and $\delta\rho_{IR}^{d}$ denote the IR contributions to the density change in tetrahedral and disrupted tetrahedral structures, respectively. By holding the SR ordering fixed within each structural type, the remaining variations in local density, $\delta\langle \rho_t \rangle$ and $\delta\langle \rho_d \rangle$, can be attributed entirely to changes in IR ordering, giving rise to $\delta\rho_{IR}^{t}$ and $\delta\rho_{IR}^{d}$. The prefactors are defined as $A = \rho^2 / \langle \rho_t \rangle \langle \rho_d \rangle$ and $k = \langle \rho_d \rangle / \langle \rho_t \rangle$, both of which vary weakly with temperature and can be treated as constants over the studied temperature range (see Supplementary Text and fig. S2). The total cumulative change in density with respect to temperature can be obtained by integrating Eq. 2

$$\Delta\rho_{total} = \int_{T_{melt}}^{T} \delta\rho(T') \ dT' = \Delta\rho_{SR} + \Delta\rho_{IR}^{t} + \Delta\rho_{IR}^{d} \quad (3)$$

The calculated contributions are shown in Fig. 1D.

Density variation from SR ordering in the H-bond network

The intrinsic density fluctuations in the H-bond network is driven by the dynamic and directional nature of hydrogen bonding, which continuously interconverts water molecules between tetrahedral structures with local density $\langle \rho_t \rangle$ and disrupted tetrahedral structures with local density $\langle \rho_d \rangle$, through the breaking and reformation of H-bonds. At temperatures below TMD, SR ordering in water is dominated by near-tetrahedral arrangements. The Voronoi cell associated with this locally ordered structure forms a compact polyhedron of volume $\langle V_t \rangle$ surrounding the central molecule, as schematically illustrated in the inset of Fig. 2A. At elevated temperatures, thermal fluctuation weakens and breaks H-bonds, disrupting the SR H-bond network. As the number of broken H-bonds grows, molecules that were previously H-bonded to the central molecule are displaced from the first coordination shell into interstitial regions as nonbonded neighbors, turning into disrupted tetrahedral arrangements. The associated Voronoi cell

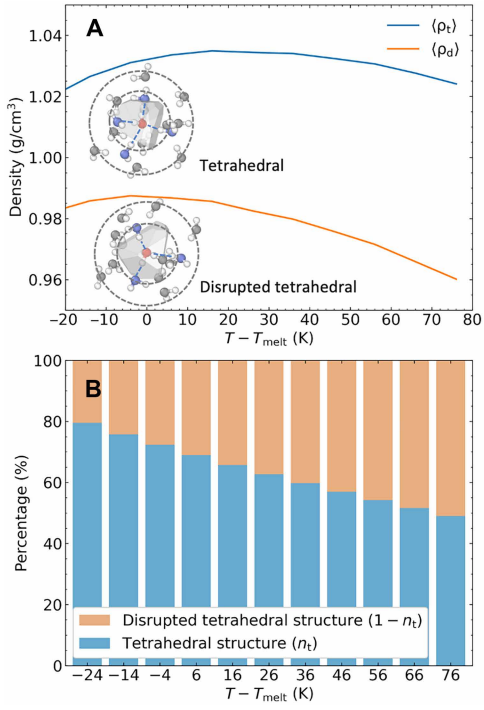

Fig. 2. SR ordering in the H-bond network. (**A**) Temperature-dependent local densities of tetrahedral ($\langle \rho_t \rangle$) and disrupted tetrahedral ($\langle \rho_d \rangle$) structures. Insets show the representative molecular structures for each structural type. The disrupted tetrahedral structure exhibits a larger Voronoi cell volume. (**B**) Temperature-dependent population fractions of tetrahedral (n_t) and disrupted tetrahedral structures ($1 - n_t$).

expands to a larger volume $\langle V_d \rangle$ with increased open space, leading to a lower local density $\langle \rho_d \rangle$, as shown in Fig. 2A. The local density $\langle \rho_t \rangle$ is consistently higher than $\langle \rho_d \rangle$, resulting in a positive gap between $\langle \rho_t \rangle$ and $\langle \rho_d \rangle$ across the entire temperature range studied. This is expected, as local density is primarily influenced by the packing of nearest neighbors, governed by the SR ordering.

With increasing temperature, the fraction n_t of water molecules exhibiting near-tetrahedral local ordering (and higher local density $\langle \rho_t \rangle$) decreases, while the fraction $1 - n_t$ corresponding to disrupted tetrahedral structures (and lower local density $\langle \rho_d \rangle$) increases, as shown in Fig. 2B. This structural shift thus results in a monotonic decrease in the density variations from changes in SR ordering $\Delta\rho_{SR}$, as shown in Fig. 1D. The sharp decline reflects substantial changes in molecular packing within the H-bond network at SR, underscoring the important role of SR ordering in governing water's density anomaly. Furthermore, the approximately linearly decreasing trend of $\Delta\rho_{SR}$ with temperature is also anticipated, given that the characteristic energy of hydrogen bonding is roughly two orders of magnitude greater than the thermal energy over the temperature range considered, placing the system firmly within the linear response regime. Nevertheless, despite its significant magnitude, the density change arising from SR H-bond ordering alone cannot account for the emergence of TMD, which requires a nonmonotonic density variation with respect to temperature.

Density variation from IR ordering in the H-bond network

With the SR ordering constrained as tetrahedron in $\Delta\rho_{IR}^{t}$ and disrupted tetrahedron in $\Delta\rho_{IR}^{d}$, respectively, $\Delta\rho_{IR} = \Delta\rho_{IR}^{t} + \Delta\rho_{IR}^{d}$ can be

unambiguously attributed to density variations arising from the IR ordering in the H-bond network. In contrast to the nearly linear decrease in $\Delta\rho_{SR}$, the IR contribution $\Delta\rho_{IR}$ exhibits a pronounced turnover as a function of temperature, as shown in Fig. 1D. This nonmonotonic behavior is crucial for the emergence of TMD in water.

A closer examination in Fig. 1D further reveals that the turnover effect in $\Delta\rho_{IR}$ is mainly driven by the component of $\Delta\rho^{t}_{IR}$ with strong nonmonotonic curvature. It indicates that the density maximum mainly originates from H-bond structural change at IR, however, with near-ideal tetrahedron at SR. The density variation in $\Delta\rho^{t}_{IR}$ is contributed by two effects, $\Delta\rho^{t}_{IR} = \Delta\rho^{t^{(-)}}_{IR} + \Delta\rho^{t^{(+)}}_{IR}$, which influence density in opposite directions, as illustrated in Fig. 3B (see the Structural analysis section in Materials and Methods for computational details). As temperature increases, the density decrement associated with $\Delta\rho^{t^{(-)}}_{IR}$ is attributed to the softening of H-bonds. This geometric softening leads to an increased H-bond length $d_{HO\cdots H}$ between neighboring water molecules, as evidenced by a shift in the center-of-mass distribution of H-bonded neighbors to larger separations (see Fig. 3A). Notably, H-bond softening perturbs the geometry of the network without breaking its connectivity, thus preserving the SR H-bond ordering. However, it affects the IR structure, causing a nearly homogeneous expansion of the Voronoi cells of each water molecule, thereby has a negative effect on the local density $\langle\rho_t\rangle$ and contributes decreasing $\Delta\rho^{t^{(-)}}_{IR}$, as schematically shown in Fig. 3B.

Conversely, the term $\Delta\rho^{t^{(+)}}_{IR}$ contributes to an increase in density with rising temperature, as shown in Fig. 3B. This density increase originates from the collapse of the H-bond network at IR. Upon heating water above its melting point, the H-bond network undergoes a fundamental transformation at the IR, due to the highly dynamic nature of hydrogen bonding. In contrast to the near-ideal tetrahedral network in crystalline ice, the second coordination shell in water begins to partially collapse, as evidenced by the diminishing second peak in the oxygen-oxygen PDF $g_{OO}(r)$ (see Fig. 3A). As this collapse progresses, water molecules at IR become nonbonded and leave the second shell, filling the interstitial region. As a result, the mass centers of IR neighbors shift inward toward the central molecule as seen in Fig. 3A, leading to a decrease in Voronoi cell volumes, as schematically plotted in the inset of Fig. 3A. As shown in Fig. 3B, $\Delta\rho^{t^{(+)}}_{IR}$ rises rapidly at low temperatures, which is attributed to the initially relatively empty interstitial region. This increment slows at higher temperatures, as the population of interstitial water molecules approaches saturation (*6*). This structural transformation is also effectively characterized by the local structure index (LSI) (*54*), as shown in Fig. 3B. The LSI here is computed exclusively for central water molecules adopting a tetrahedral structure, thus has a high correlation with the IR ordering. The temperature dependence of the LSI closely follows the trend of $\Delta\rho^{t^{(+)}}_{IR}$, providing strong support for the proposed mechanism.

During the above process, in the softened and increasingly disordered structure, the role of directional H-bonds as the dominant cohesive force diminishes. In turn, vdW interactions, although weaker, become relatively more important in stabilizing the liquid phase. Because of their nondirectional nature, vdW interactions can attract and confine those non–H-bonded water molecules that have moved out of the second shell (*18*, *55*). Here, vdW interactions play a critical role—without them, the density increment in $\Delta\rho^{t^{(+)}}_{IR}$ would be absent, and the density anomaly would not occur (see Supplementary Text and fig. S4).

Comparatively, the turnover behavior in $\Delta\rho^{d}_{IR}$ is much weaker, exhibiting a relatively flat profile near the TMD. This indicates that the H-bond network associated with locally disrupted tetrahedral ordering and a collapsed second coordination shell at IR contributes far less to the density maximum of liquid water, making further modifications to the conventional Bernal-Fowler picture. Because of the disrupted SR ordering, the interstitial region becomes populated with nonbonded water molecules originating from the broken tetrahedra. As a result, the density increase because the collapse of the IR H-bond network is strongly limited by the rapid saturation of interstitial water molecules (see Supplementary Text and fig. S5). When $\Delta\rho^{d}_{IR}$ is completely neglected, the resulting temperature and density at the maximum density point are barely changed (by 0.15 K and 0.005 g/cm^3, respectively).

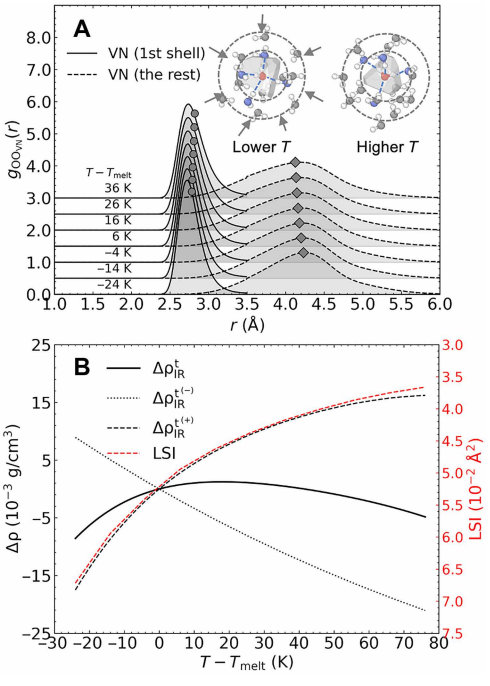

Fig. 3. IR ordering in the H-bond network. (**A**) Temperature-dependent PDFs between a central water molecule forming a tetrahedral structure and its Voronoi neighbors. Each PDF is decomposed into contributions from Voronoi neighbors in the first coordination shell and those beyond it, with circles and diamonds indicating the average radial positions of each group, respectively. Average radial positions and corresponding SD values for each temperature are provided in table S1. Insets illustrate how the accumulation of interstitial water molecules (between the two gray circles) leads to a reduction in the Voronoi cell volume of the central molecule at higher temperatures. Arrows indicate the inward movement of water molecules at IR. (**B**) Decomposition of IR density change of tetrahedral structures $\Delta\rho^{t}_{IR}$ into $\Delta\rho^{t^{(-)}}_{IR}$ and $\Delta\rho^{t^{(+)}}_{IR}$. The corresponding local structure index (LSI) is shown on the right axis in red.

DISCUSSION

By combining machine-learning molecular dynamics with a range-separated analysis of the H-bond network, we provide a microscopic explanation for the density anomaly of water. Previous theoretical efforts have largely focused on identifying local order parameters (*21*–*23*) that distinguish high- and low-density local environments. While these approaches have provided valuable qualitative insight,

they primarily offer structural classification and do not explicitly quantify how H-bond ordering at different length scales contributes cooperatively to density variations. In contrast, our analysis introduces an explicit decomposition of density changes into SR and IR structural contributions. Our results reveal that changes in SR ordering within the H-bond network alone are insufficient to account for the observed density anomaly; rearrangements in IR ordering are indispensable. In particular, we find that the nonmonotonic density behavior near the TMD arises primarily from a specific structural configuration in the H-bond network—characterized by a collapsed second coordination shell but a nearly ideal tetrahedral arrangement at SR. This configuration yields the most compact molecular packing and thus the greatest density increase near the TMD. This explains why the TMD of water lies just above its melting point, where most water molecules remain tetrahedral, but the H-bond network begins to partially collapse.

Our analysis also provides insight into the conditions under which the density anomaly vanishes. In aqueous electrolyte solutions, increasing ion concentration progressively disrupts the H-bond network and reduces the space available for water molecules to form structured coordination shells. We estimate that the density anomaly disappears when the average ion-ion distance becomes too small to form two complete coordination shells around each water molecule, which is an essential condition for the density anomaly to occur. Assuming a uniform distribution of ions, we estimate the critical concentration at which this structural disruption occurs by requiring that the average ion-ion distance equals the characteristic radius encompassing two coordination shells (~4.5 Å). This yields an estimated threshold concentration of 2.3 mol/kg for NaCl, consistent with experimental observations, where the TMD vanishes at 2.33 mol/kg (*56*). This agreement supports the proposed mechanism linking IR H-bond structuring to the presence of the density anomaly. To our knowledge, such a quantitative prediction of the critical concentration at which the density anomaly disappears has not been provided by previous theoretical frameworks. Overall, this work offers a quantitative and transferable framework for connecting local structure to macroscopic thermodynamic anomalies, with potential applications for other anomalous liquids.

MATERIALS AND METHODS

AIMD simulation

To generate the training dataset for deep potential molecular dynamics (DPMD) models, a series of Car-Parrinello (CP) (*25*) AIMD simulations of liquid water was conducted at atmospheric pressure and different temperatures within the isobaric-isothermal (NpT) ensemble in Quantum ESPRESSO (*57*). A hierarchy of different exchange-correlation functionals with increasing accuracy was adopted, including the semilocal Perdew–Burke–Ernzerhof (PBE)-generalized gradient approximation (GGA) (*40*) functional, the PBE functional with Tkatchenko-Scheffler (TS) (*44*) vdW corrections (PBE + vdW), and the hybrid version of the PBE functional (*41*, *42*) with TS-vdW corrections (PBE0 + vdW) that includes 25% exact exchange. The simulations were performed with periodically replicated cubic simulation cells containing 128 water molecules and Parrinello-Rahman barostat (*58*) constraining the cell fluctuations to be isotropic. The trajectory length of each functional at a specific temperature is listed in table S2.

The exact exchange in the PBE0 + vdW simulations is efficiently computed with maximally localized Wannier function (MLWF) in real space as described in (*43*). To efficiently compute the exact exchange energy at every AIMD step, the required MLWFs were evaluated by minimizing the total spread using second-order damped CP dynamics (*59*) and efficient on-the-fly localization of MLWFs (*60*). During this procedure, we used a fictitious mass of 500 atomic units (au), a damping coefficient of 0.3, and a time step of 4 au. Details on the implementation and convergence of exact exchange energy, force, and stress tensor are given here (*61*, *62*). The key parameters used here to achieve accurate exact exchange energy [within 0.02% off the fully converged energy (*61*)] are the following: (i) the maximum distance between a pair of MLWF centers (R_{pair}) = 8 bohr, (ii) the radius for solving Poisson equation (R_{PE}) for self-pair exchange = 6 bohr and for non–self-pair exchange = 5 bohr, and (iii) the radius for multipole expansion (R_{ME}) for self-pair exchange = 10 bohr and for non–self-pair exchange = 7 bohr.

The CP equations of motion for the nuclear and electronic degrees of freedom were integrated using the standard Verlet algorithm and a time step of 2.0 au (≈0.05 fs). The ionic temperatures were controlled with Nosé-Hoover chain thermostats (*63*), each with a chain length of 4 and a frequency of 60 THz. To achieve rapid equipartition of the thermal energy, we used one Nosé-Hoover chain thermostat per atom (i.e., the so-called "massive" Nosé-Hoover thermostat) and also rescaled the fictitious thermostat masses by the atomic masses, so that the relative rates of the thermostat fluctuations were inversely proportional to the masses of the atoms to which they were coupled (*64*).

The core electrons were treated with optimized norm-conserving Hamann-Schlüter-Chiang-Vanderbilt pseudopotentials (*65*, *66*), while the valence (pseudo–)wave functions were represented explicitly with a plane wave basis set. The electronic wave functions were expanded using a plane wave basis set with a kinetic energy cutoff of 130 rydberg (Ry). To ensure an adiabatic separation between the electronic and nuclear degrees of freedom in the CP dynamics, we used a fictitious electronic mass of 100 au and the nuclear mass of deuterium for each hydrogen atom. Mass preconditioning was applied to all Fourier components of the electronic wave functions having a kinetic energy greater than 25 Ry (*59*). To maintain a constant plane wave kinetic energy cutoff of 130 Ry during the NpT simulation, we followed the procedure of Bernasconi *et al.* (*67*) by choosing the following: (i) a cubic reference cell (with L = 30.62 bohr) that is large enough to cover the fluctuations along each lattice vector of the simulation cell throughout the NpT trajectories and (ii) a corresponding plane wave basis set with a larger kinetic energy cutoff of 150 Ry. During the NpT simulation, plane waves with a kinetic energy beyond the desired cutoff of 130 Ry were smoothly penalized by changing

$$G^2 \rightarrow G^2 + A\left[1+\text{erf}\left(\frac{\frac{1}{2}G^2 - E_0}{\sigma}\right)\right] \tag{4}$$

with a judicious choice of parameters (A = 200 Ry, σ = 15 Ry, E_0 = 130 Ry); this modification to G^2 causes the higher-energy (>130 Ry) plane waves to become essentially inactive basis functions in the description of the valence (pseudo–)wave functions and thereby leads to NpT dynamics, which mimic a constant plane wave cutoff of ≈130 Ry.

Although a linear-scaling exact-exchange algorithm (*43*) was applied to reduce the computational burden of PBE0 + vdW calculations, the computation cost is still much higher than PBE and PBE + vdW calculations. Therefore, 48-ps PBE0 + vdW AIMD simulations

are conducted, which are much shorter than the 216.6-ps PBE trajectory and the 372.3-ps PBE + vdW trajectory as shown in table S2. As the structure of liquid water predicted by PBE0 + vdW is softer than the other two functionals, the 48-ps trajectory can cover most of the potential energy surface and produce a relatively converged deep potential model.

DPMD simulation

We used the Deep Potential Molecular Dynamics (DeePMD) framework (*34*–*36*) to perform simulations of liquid water. For each functional, the deep potential model is trained independently using the corresponding AIMD trajectories. The atomic position, total potential energy E, ionic forces $\mathbf{F}_i$, and the stress tensor Ξ at each time step were extracted from the AIMD trajectories and adopted as the input training data for the DPMD model. The training was conducted for 10^6 steps using the DeePMD-kit package (*36*) interfaced with the TensorFlow library (*68*) following the procedure described in (*34*, *69*). First, the input data were transformed to local coordinate frames for every atom and its neighbors inside a cutoff distance of 6 Å to preserve the translational, rotational, and permutational symmetries of the environment. This cutoff is sufficiently large to encompass the dominant contributions from H-bond networks and vdW interactions in liquid water and is consistent with the density-density correlation length of liquid water reported in previous theoretical studies (*51*). Then, the Adam method (*70*) was applied to optimize the deep neural network parameters with the loss function

$$\mathcal{L}\left(p_\epsilon, p_f, p_\xi\right) = p_\epsilon \Delta\epsilon^2 + \frac{p_f}{3N}\sum_i |\Delta\mathbf{F}_i|^2 + \frac{p_\xi}{9}\|\Delta\xi\|^2 \quad (5)$$

where $\Delta\epsilon$, $\Delta\mathbf{F}_i$, and $\Delta\xi$ represent the differences between the training data and current DPMD prediction for the quantities $\epsilon \equiv E/N$, $\mathbf{F}_i$, and $\xi \equiv \Xi/N$, respectively; N is the number of atoms, and p_ϵ, p_f, and p_ξ are tunable prefactors. In the training process, p_ϵ progressively increases from 0.02 to 1, while p_f progressively decreases from 1000 to 1 for all three DPMD models. The prefactor of the stress, p_ξ, progressively increases from 0.02 to 1 for the PBE model, while p_ξ was set to zero in the training progress of PBE + vdW and PBE0 + vdW models. The resulting root mean square error between the energy predicted by the PBE and PBE + vdW (PBE0 + vdW) DPMD models and that predicted by AIMD is smaller than 0.4 (0.8) meV per atom.

The obtained DPMD models were applied to conduct DPMD simulations using the DeePMD-kit package (*36*). For each exchange-correlation functional, a series of DPMD simulations was carried out in the NPT ensemble at atmospheric pressure and temperatures from 290 to 390 K, with 10-K intervals. Considering that PBE does not show a density maximum in 290 to 390 K, the simulated temperature range for PBE was extended to 270 to 390 K. The cell size was enlarged to 1024 water molecules, and the simulation lasted for 2 ns at each thermodynamic condition with a timestep of 0.5 fs to produce converged densities and structural properties. The first 50-ps trajectories are discarded for equilibration.

To determine the melting temperature of ice (T_{melt}), we used the thermodynamic integration method (*71*, *72*) implemented in the Deep Potential Thermodynamic Integration (DPTI) package (*73*) to yield the absolute Gibbs free energies, G_{ice} and G_{liq}, of ice and liquid water, respectively. The melting temperature was then determined as the temperature at which these two free energies intersect, i.e., when $G_{\mathrm{ice}} = G_{\mathrm{liq}}$, indicating thermodynamic equilibrium between the solid and liquid phases. The simulated density-temperature ($\rho - T$) data were fitted to a fourth-order polynomial

$$\rho(T) = a_0 + a_1 T + a_2 T^2 + a_3 T^3 + a_4 T^4 \quad (6)$$

The TMD was determined as the temperature at which the fitted polynomial reaches its maximum by evaluating the polynomial on a refined temperature grid (0.01-K resolution). The fitted coefficients are listed in table S3. Sensitivity tests varying the polynomial order (fourth to sixth) indicated a numerical uncertainty of less than 0.2 K, which is small compared to the systematic differences between functionals and does not affect the qualitative trends or mechanistic conclusions presented.

Structural analysis

To characterize local structural fluctuations in liquid water, we performed a Voronoi tessellation of the simulation box using the voro++ library (*49*), assigning a unique spatial volume to each water molecule. H-bonds were identified using the geometric criterion introduced by Luzar and Chandler (*74*), where a H-bond is considered to exist between two water molecules if $R_{\mathrm{OO}} < 3.5$ Å and $\angle \mathrm{H_D - O_D \cdots O_A} < 30°$. Each water molecule is then classified into one of two structural categories based on its number of H-bonds. Here, water molecules with four or more H-bonds are labeled as adopting a tetrahedral structure, while those with fewer than four H-bonds categorized as having a disrupted tetrahedral structure.

At the IR, increasing temperature leads to geometric softening of H-bonds and an increase in the average H-bond length $d_{\mathrm{HO\cdots H}}$ between neighboring water molecules. This H-bond elongation results in a nearly homogeneous expansion of the Voronoi cells of each water molecule, thereby decreasing the local densities and contributing negatively to the IR component of the density change. To model this behavior, we consider an idealized tetrahedral configuration in which the central water molecule forms H-bonds with four nearest neighbors arranged in a perfect tetrahedral geometry and neglects contributions from more distant neighbors. In this simplified picture, the Voronoi cell volume can be estimated as $V_{\mathrm{est}} = \sqrt{3}\ a^3$, where a is the H-bond length, and the estimated local density $\rho_{\mathrm{est}} = m/V_{\mathrm{est}}$, where m is the molecular mass.

To evaluate the validity of this approximation, we compare the actual mean local density $\langle\rho_t\rangle$ computed from simulations with the estimated local density ρ_{est} as a function of a. As shown in fig. S1, despite the structural complexity of real liquid water, the trend in $\langle\rho_t\rangle$ closely follows the trend predicted by the ideal tetrahedral model. This observation indicates that the local density fluctuations in water are strongly correlated with changes in H-bond length. Therefore, the negative contribution to the density variation from H-bond softening in tetrahedral structures can be approximated as

$$\delta\langle\rho_t\rangle^{(-)} = \delta\rho_{\mathrm{est}} = \delta\left(\frac{m}{V_{\mathrm{est}}}\right) = \frac{-\sqrt{3}m}{a^4}\ \delta a 0 \quad (7)$$

The remaining part of the local density change, attributed to interstitial accumulation, is then estimated as $\delta\langle\rho_t\rangle^{(+)} = \delta\langle\rho_t\rangle - \delta\langle\rho_t\rangle^{(-)}$. Using Eq. 2 from the main text, the corresponding contributions to the IR component of the density change are computed as

$$\delta\rho_{\mathrm{IR}}^{\mathrm{t}(-)} = A n_t k\ \delta\langle\rho_t\rangle^{(-)}, \quad \delta\rho_{\mathrm{IR}}^{\mathrm{t}(+)} = A n_t k\ \delta\langle\rho_t\rangle^{(+)} \quad (8)$$

A similar procedure is applied to evaluate the IR contributions from disrupted tetrahedral structures.

Supplementary Materials

This PDF file includes:

Supplementary Text
Figs. S1 to S8
Tables S1 to S4

REFERENCES

1. D. Eisenberg, W. Kauzmann, *The Structure and Properties of Water* (Oxford Univ. Press, 2005).
2. J. D. Bernal, R. H. Fowler, A theory of water and ionic solution, with particular reference to hydrogen and hydroxyl ions. *J. Chem. Phys.* **1**, 515–548 (1933).
3. P. H. Poole, F. Sciortino, U. Essmann, H. E. Stanley, Phase behaviour of metastable water. *Nature* **360**, 324–328 (1992).
4. M. C. Bellissent-Funel, Is there a liquid-liquid phase transition in supercooled water? *Europhys. Lett.* **42**, 161–166 (1998).
5. C. Huang, K. T. Wikfeldt, T. Tokushima, D. Nordlund, Y. Harada, U. Bergmann, M. Niebuhr, T. M. Weiss, Y. Horikawa, M. Leetmaa, M. P. Ljungberg, O. Takahashi, A. Lenz, L. Ojamäe, A. P. Lyubartsev, S. Shin, L. G. M. Pettersson, A. Nilsson, The inhomogeneous structure of water at ambient conditions. *Proc. Natl. Acad. Sci. U.S.A.* **106**, 15214–15218 (2009).
6. A. K. Soper, M. A. Ricci, Structures of high-density and low-density water. *Phys. Rev. Lett.* **84**, 2881–2884 (2000).
7. M. J. Cuthbertson, P. H. Poole, Mixturelike behavior near a liquid-liquid phase transition in simulations of supercooled water. *Phys. Rev. Lett.* **106**, 1–4 (2011).
8. B. Santra, R. A. DiStasio, F. Martelli, R. Car, Local structure analysis in ab initio liquid water. *Mol. Phys.* **113**, 2829–2841 (2015).
9. D. González-Salgado, E. G. Noya, E. Lomba, Simulation and theoretical analysis of the origin of the temperature of maximum density of water. *Fluid Phase Equilib.* **560**, 113515 (2022).
10. O. Mishima, H. E. Stanley, The relationship between liquid, supercooled and glassy water. *Nature* **396**, 329–335 (1998).
11. A. Nilsson, L. G. Pettersson, The structural origin of anomalous properties of liquid water. *Nat. Commun.* **6**, 8998 (2015).
12. J. Russo, H. Tanaka, Understanding water's anomalies with locally favoured structures. *Nat. Commun.* **5**, 3556 (2014).
13. L. Xu, P. Kumar, S. V. Buldyrev, S.-H. Chen, P. H. Poole, F. Sciortino, H. E. Stanley, Relation between the widom line and the dynamic crossover in systems with a liquid-liquid phase transition. *Proc. Natl. Acad. Sci. U.S.A.* **102**, 16558–16562 (2005).
14. H. E. Stanley, P. Kumar, G. Franzese, L. Xu, Z. Yan, M. G. Mazza, S. V. Buldyrev, S.-H. Chen, F. Mallamace, Liquid polyamorphism: Possible relation to the anomalous behavior of water. *Eur. Phys. J. Spec. Top.* **161**, 1–17 (2008).
15. H. Tanaka, Bond orientational ordering in liquids: Towards a unified description of water-like anomalies, liquid-liquid transition, glass transition, and crystallization. *Eur. Phys. J. E* **35**, 113 (2012).
16. C. H. Cho, S. Singh, G. W. Robinson, An explanation of the density maximum in water. *Phys. Rev. Lett.* **76**, 1651–1654 (1996).
17. C. Vega, J. L. Abascal, Relation between the melting temperature and the temperature of maximum density for the most common models of water. *J. Chem. Phys.* **123**, 144504 (2005).
18. T. Morawietz, A. Singraber, C. Dellago, J. Behler, How van der Waals interactions determine the unique properties of water. *Proc. Natl. Acad. Sci. U.S.A.* **113**, 8368–8373 (2016).
19. J. L. Finney, The structure of water: A historical perspective. *J. Chem. Phys.* **160**, 060901 (2024).
20. P. Gallo, K. Amann-Winkel, C. A. Angell, M. A. Anisimov, F. Caupin, C. Chakravarty, E. Lascaris, T. Loerting, A. Z. Panagiotopoulos, J. Russo, F. Sciortino, H. E. Stanley, Y. Xu, L. Xu, Water: A tale of two liquids. *Chem. Rev.* **116**, 7463–7500 (2016).
21. R. S. Singh, J. W. Biddle, P. G. Debenedetti, M. A. Anisimov, Two-state thermodynamics and the possibility of a liquid-liquid phase transition in supercooled TIP4P/2005 water. *J. Chem. Phys.* **144**, 144504 (2016).
22. E. Duboué-Dijon, D. Laage, Characterization of the local structure in liquid water by various order parameters. *J. Phys. Chem. B* **119**, 8406–8418 (2015).
23. R. Shi, H. Tanaka, Microscopic structural descriptor of liquid water. *J. Chem. Phys.* **148**, 124503 (2018).
24. H. Tanaka, H. Tong, R. Shi, J. Russo, Revealing key structural features hidden in liquids and glasses. *Nat. Rev. Phys.* **1**, 333–348 (2019).
25. R. Car, M. Parrinello, Unified approach for molecular dynamics and density-functional theory. *Phys. Rev. Lett.* **55**, 2471–2474 (1985).
26. P. Hohenberg, W. Kohn, Inhomogeneous electron gas. *Phys. Rev.* **136**, B864–B871 (1964).
27. W. Kohn, L. J. Sham, Self-consistent equations including exchange and correlation effects. *Phys. Rev.* **140**, A1133–A1138 (1965).
28. C. W. Swartz, X. Wu, Ab initio studies of ionization potentials of hydrated hydroxide and hydronium. *Phys. Rev. Lett.* **111**, 087801 (2013).
29. A. P. Gaiduk, G. Galli, Local and global effects of dissolved sodium chloride on the structure of water. *J. Phys. Chem. Lett.* **8**, 1496–1502 (2017).
30. V. Rozsa, T. A. Pham, G. Galli, Molecular polarizabilities as fingerprints of perturbations to water by ions and confinement. *J. Chem. Phys.* **152**, 124501 (2020).
31. F. Tang, J. Xu, D. Y. Qiu, X. Wu, Nuclear quantum effects on the quasiparticle properties of the chloride anion aqueous solution within the GW approximation. *Phys. Rev. B* **104**, 035117 (2021).
32. M. DelloStritto, J. Xu, X. Wu, M. L. Klein, Aqueous solvation of the chloride ion revisited with density functional theory: Impact of correlation and exchange approximations. *Phys. Chem. Chem. Phys.* **22**, 10666–10675 (2020).
33. J. Behler, M. Parrinello, Generalized neural-network representation of high-dimensional potential-energy surfaces. *Phys. Rev. Lett.* **98**, 146401 (2007).
34. L. Zhang, J. Han, H. Wang, R. Car, W. E, Deep potential molecular dynamics: A scalable model with the accuracy of quantum mechanics. *Phys. Rev. Lett.* **120**, 143001 (2018).
35. J. Han, L. Zhang, R. Car, W. E, Deep potential: A general representation of a many-body potential energy surface. *Commun. Comput. Phys.* **23**, 629–639 (2018).
36. H. Wang, L. Zhang, J. Han, W. E, DeePMD-kit: A deep learning package for many-body potential energy representation and molecular dynamics. *Comput. Phys. Commun.* **228**, 178–184 (2018).
37. R. Hou, Y. Quan, D. Pan, Dielectric constant of supercritical water in a large pressure-temperature range. *J. Chem. Phys.* **153**, 101103 (2020).
38. Y. Song, X. Wu, Pressure-induced structural and dielectric changes in liquid water at room temperature. *J. Chem. Phys.* **162**, 114508 (2025).
39. Y. Li, B. Yang, C. Zhang, R. Car, Assessing the accuracy of various exchange-correlation functionals in capturing nuclear quantum effects on the melting point of ice Ih, APS March Meeting 2024, Z60.013, March 2024.
40. J. P. Perdew, K. Burke, M. Ernzerhof, Generalized gradient approximation made simple. *Phys. Rev. Lett.* **77**, 3865–3868 (1996).
41. J. P. Perdew, M. Ernzerhof, K. Burke, Rationale for mixing exact exchange with density functional approximations. *J. Chem. Phys.* **105**, 9982–9985 (1996).
42. C. Adamo, V. Barone, Toward reliable density functional methods without adjustable parameters: The PBE0 model. *J. Chem. Phys.* **110**, 6158–6170 (1999).
43. X. Wu, A. Selloni, R. Car, Order-*N* implementation of exact exchange in extended insulating systems. *Phys. Rev. B* **79**, 085102 (2009).
44. A. Tkatchenko, M. Scheffler, Accurate molecular van der Waals interactions from ground-state electron density and free-atom reference data. *Phys. Rev. Lett.* **102**, 073005 (2009).
45. G. Kell, Precise representation of volume properties of water at one atmosphere. *J. Chem. Eng. Data* **12**, 66–69 (1967).
46. D. E. Hare, C. M. Sorensen, The density of supercooled water. II. Bulk samples cooled to the homogeneous nucleation limit. *J. Chem. Phys.* **87**, 4840–4845 (1987).
47. B. Cheng, E. A. Engel, J. Behler, C. Dellago, M. Ceriotti, Ab initio thermodynamics of liquid and solid water. *Proc. Natl. Acad. Sci. U.S.A.* **116**, 1110–1115 (2019).
48. G. Voronoi, Nouvelles applications des paramètres continus à la théorie des formes quadratiques. Deuxième mémoire. Recherches sur les parallélloèdres primitifs. *J. Reine Angew. Math.* **134**, 198–287 (1908).
49. C. H. Rycroft, VORO++: A three-dimensional Voronoi cell library in C++. *Chaos* **19**, 041111 (2009).
50. E. A. Lazar, J. Lu, C. H. Rycroft, Voronoi cell analysis: The shapes of particle systems. *Am. J. Phys.* **90**, 469–480 (2022).
51. N. J. English, J. S. Tse, Density fluctuations in liquid water. *Phys. Rev. Lett.* **106**, 1–4 (2011).
52. D. Laage, J. T. Hynes, A molecular jump mechanism of water reorientation. *Science* **311**, 832–835 (2006).
53. D. Laage, G. Stirnemann, F. Sterpone, J. T. Hynes, Water jump reorientation: From theoretical prediction to experimental observation. *Acc. Chem. Res.* **45**, 53–62 (2012).
54. K. T. Wikfeldt, A. Nilsson, L. G. Pettersson, Spatially inhomogeneous bimodal inherent structure of simulated liquid water. *Phys. Chem. Chem. Phys.* **13**, 19918–19924 (2011).
55. A. P. Gaiduk, F. Gygi, G. Galli, Density and compressibility of liquid water and ice from first-principles simulations with hybrid functionals. *J. Phys. Chem. Lett.* **6**, 2902–2908 (2015).
56. D. G. Archer, R. W. Carter, Thermodynamic properties of the $NaCl^+$ H_2O system. 4. Heat capacities of H_2O and NaCl(aq) in cold-stable and supercooled states. *J. Phys. Chem. B* **104**, 8563–8584 (2000).
57. P. Giannozzi, S. Baroni, N. Bonini, M. Calandra, R. Car, C. Cavazzoni, D. Ceresoli, G. L. Chiarotti, M. Cococcioni, I. Dabo, A. D. Corso, S. D. Gironcoli, S. Fabris, G. Fratesi, R. Gebauer, U. Gerstmann, C. Gougoussis, A. Kokalj, M. Lazzeri, L. Martin-Samos, N. Marzari, F. Mauri, R. Mazzarello, S. Paolini, A. Pasquarello, L. Paulatto, C. Sbraccia,

S. Scandolo, G. Sclauzero, A. P. Seitsonen, A. Smogunov, P. Umari, R. M. Wentzcovitch, QUANTUM ESPRESSO: A modular and open-source software project for quantum simulations of materials. *J. Phys. Condens. Matter* **21**, 395502 (2009).
58. M. Parrinello, A. Rahman, Crystal structure and pair potentials: A molecular-dynamics study. *Phys. Rev. Lett.* **45**, 1196–1199 (1980).
59. F. Tassone, F. Mauri, R. Car, Accelerated molecular dynamics for metallic systems. *Phys. Rev. B* **50**, 10561–10573 (1994).
60. M. Sharma, Y. Wu, R. Car, Ab initio molecular dynamics with maximally localized Wannier functions. *Int. J. Quantum Chem.* **95**, 821–829 (2003).
61. H.-Y. Ko, J. Jia, B. Santra, X. Wu, R. Car, R. A. DiStasio Jr., Enabling large-scale condensed-phase hybrid density functional theory based ab initio molecular dynamics. 1. Theory, algorithm, and performance. *J. Chem. Theory Comput.* **16**, 3757–3785 (2020).
62. H.-Y. Ko, B. Santra, R. A. DiStasio Jr., Enabling large-scale condensed-phase hybrid density functional theory-based ab initio molecular dynamics ii: Extensions to the isobaric–isoenthalpic and isobaric–isothermal ensembles. *J. Chem. Theory Comput.* **17**, 7789–7813 (2021).
63. G. J. Martyna, M. L. Klein, M. Tuckerman, Nosé-Hoover chains: The canonical ensemble via continuous dynamics. *J. Chem. Phys.* **97**, 2635–2643 (1992).
64. D. J. Tobias, G. J. Martyna, M. L. Klein, Molecular dynamics simulations of a protein in the canonical ensemble. *J. Phys. Chem.* **97**, 12959–12966 (1993).
65. D. R. Hamann, M. Schlüter, C. Chiang, Norm-conserving pseudopotentials. *Phys. Rev. Lett.* **43**, 1494–1497 (1979).
66. D. Vanderbilt, Optimally smooth norm-conserving pseudopotentials. *Phys. Rev. B* **32**, 8412–8415 (1985).
67. M. Bernasconi, G. L. Chiarotti, P. Focher, S. Scandolo, E. Tosatti, M. Parrinello, First principles simulation of liquid and amorphous Si. *J. Phys. Chem. Solid* **56**, 501–505 (1995).
68. M. Abadi, P. Barham, J. Chen, Z. Chen, A. Davis, J. Dean, M. Devin, S. Ghemawat, G. Irving, M. Isard, M. Kudlur, J. Levenberg, R. Monga, S. Moore, D. G. Murray, B. Steiner, P. Tucker, V. Vasudevan, P. Warden, M. Wicke, Y. Yu, X. Zheng, "TensorFlow: A System for Large-Scale Machine Learning," in *12th USENIX Symposium on Operating Systems Design and Implementation (OSDI)* (USENIX Association, 2016), pp. 265–283.
69. L. Zhang, J. Han, H. Wang, W. Saidi, R. Car, W. E, "End-to-end symmetry preserving inter-atomic potential energy model for finite and extended systems," in *Advances in Neural Information Processing Systems 31 (NeurIPS)*, S. Bengio, H. Wallach, H. Larochelle, K. Grauman, N. Cesa-Bianchi, R. Garnett, Eds. (Curran Associates Inc., 2018), pp. 4436–4446.
70. D. P. Kingma, J. Ba, Adam: A method for stochastic optimization. arXiv:1412.6980 [cs.LG] (2017).
71. D. Frenkel, A. J. C. Ladd, New Monte Carlo method to compute the free energy of arbitrary solids. Application to the fcc and hcp phases of hard spheres. *J. Chem. Phys.* **81**, 3188–3193 (1984).
72. L. Zhang, H. Wang, R. Car, W. E, Phase diagram of a deep potential water model. *Phys. Rev. Lett.* **126**, 236001 (2021).
73. Deep Potential Toolkit (DPTI) (2024); https://github.com/deepmodeling/dpti.
74. A. Luzar, D. Chandler, Hydrogen-bond kinetics in liquid water. *Nature* **379**, 55–57 (1996).

Acknowledgments

Funding: This research was supported by the Computational Chemical Center: Chemistry in Solution and at Interfaces, funded by the US Department of Energy (DOE) under award no. DE-SC0019394. Computational resources were provided by the National Energy Research Scientific Computing Center (NERSC), a DOE Office of Science User Facility, operated under contract no. DE-AC02-05CH11231. This work was partially supported by the National Science Foundation through grant no. DMR-2053195 and Seven Research LLC. **Author contributions:** Conceptualization: Y.S., R.L., X.W., and M.L.K. Methodology: Y.S., R.L., C.Z., Y.L., and B.S. Software: R.L., Y.L., and B.S. Validation: R.L. and B.S. Formal analysis: R.L. and B.S. Investigation: Y.S. and R.L. Data curation: R.L. and B.S. Visualization: Y.S. Resources: R.L., X.W., and M.L.K. Supervision: M.C., M.L.K., and X.W. Project administration: X.W. Funding acquisition: X.W. and M.L.K. Writing—original draft: Y.S., B.S., and X.W. Writing—review and editing: Y.S., Y.L., and X.W. **Competing interests:** The authors declare that they have no competing interests. **Data, code, and materials availability:** All data and code needed to evaluate and reproduce the results in the paper are present in the paper and/or the Supplementary Materials. In addition, the machine-learned potentials, processed data, example analysis scripts, and a representative configuration snapshot are publicly available at Dryad: https://datadryad.org/dataset/doi:10.5061/dryad.bvq83bkqm. This study did not generate new materials.

Submitted 4 October 2025
Accepted 17 April 2026
Published 27 May 2026
10.1126/sciadv.aec6748

ScienceAdvances

Understanding the density maximum of water with machine-learned potentials

Yizhi Song, Renxi Liu, Chunyi Zhang, Yifan Li, Biswajit Santra, Mohan Chen, Michael L. Klein, and Xifan Wu

Sci. Adv. **12** (22), eaec6748. DOI: 10.1126/sciadv.aec6748

Science Advances (ISSN 2375-2548) is published by the American Association for the Advancement of Science. 1200 New York Avenue NW, Washington, DC 20005. The title *Science Advances* is a registered trademark of AAAS.